RSC Advances

ROYAL SOCIETY
OF CHEMISTRY

PAPER

View Article Online
View Journal | View Issue

Check for updates

Cite this: *RSC Adv.*, 2026, **16**, 7481

Multiphysics model for designing magnetic bead collection processes on centrifugal microfluidic platforms

Jakob Wimmer,[ab] Carole Planchette, [c] Gerhard A. Holzapfel [ade]
and Theresa Rienmüller *[ae]

Received 19th December 2025
Accepted 19th January 2026

DOI: 10.1039/d5ra09842d

rsc.li/rsc-advances

Immunoassays require high sensitivity and specificity for the detection of low-abundance analytes in complex matrices such as blood plasma. The use of functionalized magnetic beads can increase assay sensitivity by selectively binding and concentrating target analytes, facilitating their separation. However, magnetophoretic bead collection still represents a critical bottleneck. It must be performed repeatedly throughout sequential mixing, washing, and dilution steps, which is time-consuming and prone to cumulative bead loss, ultimately reducing assay performance. Here, we present a comprehensive framework for the design of magnetic bead collection systems integrated on a rotating microfluidic (lab-on-a-disc) platform. We establish a finite-element multiphysics model of bead collection that couples magnetophoretic forces, centrifugal effects, magnetophoresis-induced convection, and cooperative bead motion. The model is experimentally validated on a dedicated setup using Dynabeads M270. Increased bead collection speed is attributed to convection-enhanced transport and bead aggregation into chains. The model enables systematic investigation of geometric parameters, fluid viscosity, bead properties, and rotational protocols, as well as the efficiency of various permanent magnet configurations. We investigate magnet arrangements, vary the rotational speed between 300 and 800 rpm, and the magnet-fluid distance between 2 and 6 mm. Within this range, our results show, for any targeted collection fraction, a linear decrease in collection time with increasing magnet-fluid distance and an exponential reduction with decreasing rotational speed. Beyond performance gains, this predictive *in silico* framework reduces the reliance on costly trial-and-error optimization and can accelerate assay development.

1 Introduction

Centrifugal microfluidic platforms have established themselves as a robust, automated solution for point-of-care diagnostics, enabling rapid testing at the site of care. These systems utilize a rotating microfluidic disc placed within a dedicated instrument to control rotation, thermal management, and optical detection. A key advantage of these systems over conventional microfluidic chips is the automation of complex fluid handling through precise rotational control, eliminating the need for external pumps or valves. By integrating assay reagents on the disc, these platforms can perform various diagnostic protocols, including immunoassays[1] and molecular diagnostics,[2] with minimal user intervention.[3,4] Immunoassays require high sensitivity and specificity for the detection of target analytes, which are often present at low concentrations in complex samples like blood plasma. Magnetic beads functionalized with specific biomolecules are frequently used to enrich and purify these analytes by selectively binding them from the sample. Applying a magnetic field draws them toward a defined region, a process referred to as bead collection in this study. This magnetically driven bead collection step concentrates and separates the target molecules while leaving unwanted components dispersed in the bulk, thereby increasing assay sensitivity and reducing non-specific interactions.[5–7]

In a typical workflow, target molecules first bind to the functionalized magnetic beads during an incubation step, forming bead–analyte complexes (see Fig. 1A). After this binding step, a magnetic field is applied with permanent magnets to collect the beads in a defined region (Fig. 1B), allowing the bulk fluid to be aspirated and discarded. A robust collection (left) is essential to quickly and efficiently concentrate the beads, enabling subsequent washing steps without

---

[a] *Institute of Biomechanics, Graz University of Technology, Graz, Austria. E-mail: theresa.rienmueller@tugraz.at*

[b] *Erba Technologies Austria GmbH, Graz, Austria*

[c] *Institute of Fluid Mechanics and Heat Transfer, Graz University of Technology, Graz, Austria*

[d] *Department of Structural Engineering, Norwegian University of Science and Technology (NTNU), Trondheim, Norway*

[e] *BioTechMed-Graz, Graz, Austria*

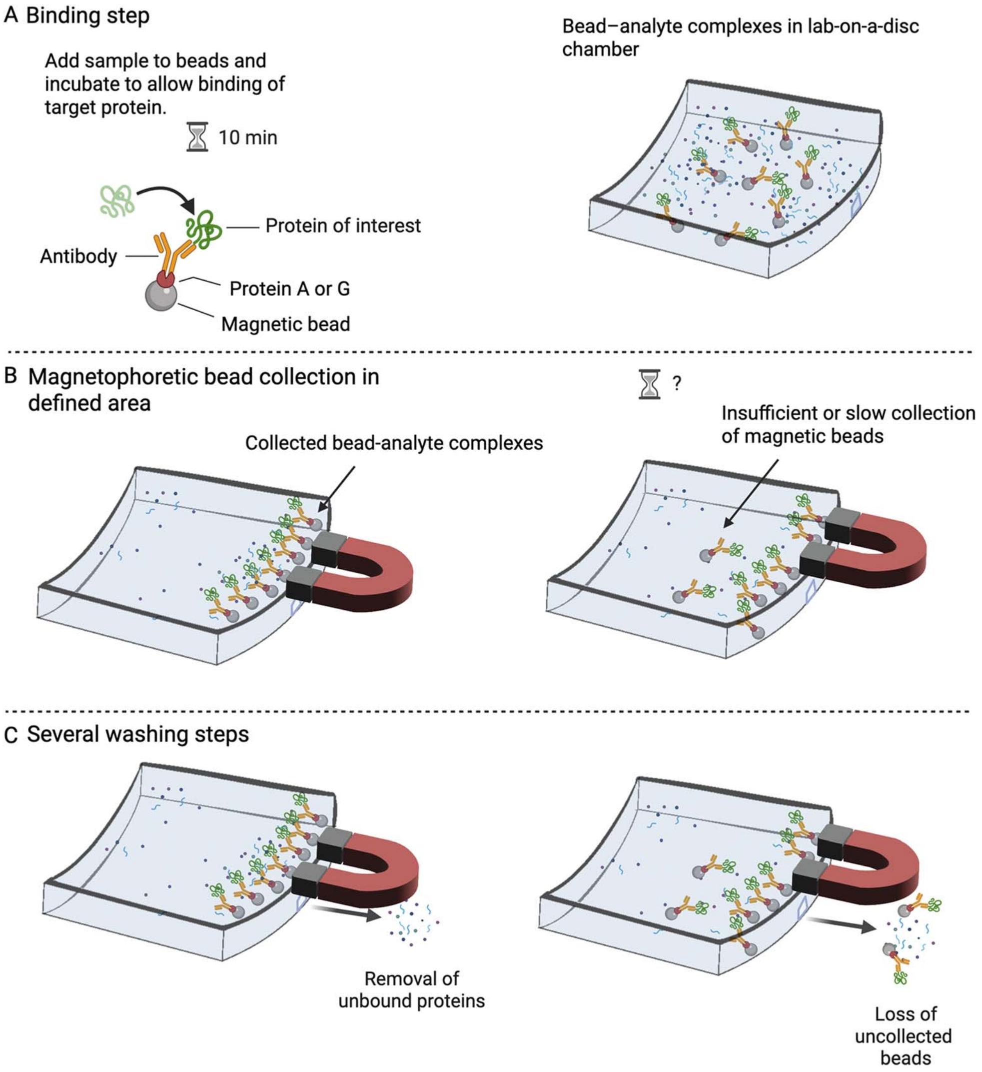

Fig. 1 Typical workflow of magnetic bead-based lab-on-a-disc assays. (A) The antibodies are incubated with the magnetic beads and the sample to be analyzed to form bead-analyte complexes. (B) Permanent magnets are used to collect the beads in a defined region magnetically. (C) Several consecutive steps of collection, washing, re-suspension, and washing are typically performed. With efficiently collected beads (left), this results in bounded analyte purification, while ineffectively collected beads (right) are partially washed out, potentially leading to a loss of assay sensitivity. Created in BioRender. Rienmüller T. (2026) https://BioRender.com/qplyk0c.

significant bead loss (Fig. 1C). Depending on the specific assays, several successive collection, washing and resuspension steps can be applied to reach appropriate analyte purification. In the last step, an elution buffer is applied to release the target analytes and make them available for downstream detection.[5,8,9]

Magnetic beads have become an attractive solid phase for ELISA workflows because they can both accelerate immunoreactions and improve analytical sensitivity. In particular, well-dispersed antibody-conjugated beads provide a high surface-area-to-volume ratio, which promotes faster antigen–antibody binding. In addition, the beads can be rapidly manipulated with an external magnet so that bead–analyte complexes are efficiently separated and pre-concentrated. As highlighted by Ha and Kim,[5] this magnetic preconcentration step is a key contributor to assay sensitivity, because the bead–analyte complexes must first be collected by an external magnet and re-dispersed into a smaller volume to effectively enhance the detectable analyte concentration. However, in practical laboratory and point-of-care settings, the performance of magnetic bead-based assays often faces challenges such as incomplete bead mixing, low or inconsistent bead collection, or bead loss during aspiration. If the beads are not collected reliably and within a sufficiently short time, a fraction of them may remain dispersed in the chamber and be washed away together with the supernatant (Fig. 1C (right)), which directly compromises the amount of bead-bound analytes available for downstream processing. These issues can negatively affect the sensitivity and reproducibility, and sample loss during magnetic-bead–based extraction has indeed been identified as a contributor to reduced assay sensitivity.[7,10] Moreover, bead collection is typically performed multiple times during sequential binding and washing steps. If each collection step is slow or poorly optimized, the cumulative collection time can become comparable to the biochemical incubation itself, limiting overall assay throughput. By contrast, very rapid and robust bead collection reduces dead time between incubation and washing, which is beneficial for time-resolved measurements.[11] Reciprocally, in systems designed for fast collection, models that do not properly account for convection and cooperative bead effects are prone to substantial errors, highlighting the need for validated quantitative models of the collection step that include these mechanisms.[12–15]

Several studies have examined aspects of magnetic bead behavior, but each addresses only a subset of the mechanisms relevant for reliable bead collection on a rotating disc. A seminal contribution by Kirby *et al.*[16] introduced centrifugo-magnetophoretic particle separation on lab-on-a-disc platforms and modeled the underlying magnetic and centrifugal forces, but did not resolve cooperative bead aggregation or use in realistic chamber geometries. Building on this, Strohmeier *et al.*[17] simulated the magnetic forces acting on beads in lab-on-a-disc geometries, yet likewise they did not evaluate the resulting bead-collection dynamics under rotation. Other studies focused on magnetophoresis-induced convection, such as the mathematical framework presented by[18] and the simulation work by,[19] which analyzed the flow patterns generated by magnetophoretic forces, but did not quantify bead transport or accumulation. Complementary studies have examined magnetic bead chain formation behavior in polymer solutions or bulk fluids (*e.g.*,[20]), yet these investigations were not performed in centrifugal microfluidic geometries and did not consider the superposition of magnetic, convective, and centrifugal effects in a unified framework. More general reviews of magnetophoresis-based microfluidics similarly highlight the complexity of coupling magnetic forces, flow, and particle interactions, and point to the need for quantitatively validated models in realistic device architectures.[13]

Collectively, these contributions provide valuable insights into magnetic force fields, magnetically driven convection, and bead chain formation, but none of them quantify how rotation speed, convection, and magnet configuration jointly determine bead collection fraction and accumulation behavior, in a lab-on-a-disc environment.

To address this gap, we develop a finite-element multiphysics framework for the design, simulation, and optimization of magnetophoretic bead collection on a centrifugal microfluidic platform. The model incorporates the relevant phenomena governing bead motion on lab-on-a-disc systems, including magnetic forces, fluid drag, centrifugal forces, and collective effects, enabling a realistic three-dimensional description of bead behavior under rotation with permanent magnets. In contrast to previous models, which often rely on oversimplified assumptions (see, *e.g.* ref. 19 and 21) or 2D approximations, our approach allows quantitative prediction of collection speed, efficiency, and bead accumulation patterns across a wide range of operating parameters.

COMSOL Multiphysics is used to simulate the magnetic bead collection process, enabling systematic evaluation of different magnet configurations and rotational speeds. We experimentally validate the model on a dedicated rotating platform by comparing simulation results with absorption-based measurements, which provide space- and time-resolved estimates of the particle concentration within the collection chamber. Through combined mathematical modeling, simulation, and experimental validation, we present a generalizable tool for investigating and characterizing magnetophoretic bead-collection dynamics on centrifugal platforms. This framework enables informed design decisions and supports the development of reliable bead-based microfluidic architectures.

2 System design

2.1 Experimental setup for magnetic bead collection

The collection mechanism for our lab-on-a-disc setup consists of a ring of permanent magnets positioned axially above the disc, as shown in Fig. 2A. The arrangement of at least four magnets along the ring suppresses the need to spin them above the disc as proposed by Ouyang *et al.*,[22] who used only two magnets. Further and in contrast to the design by Hin *et al.*,[23] this magnetic ring can be moved axially (vertical arrow in Fig. 2A), allowing selective interaction with the magnetic beads. With sufficient proximity, the ring attracts the beads to the top of the chamber and holds them radially in place. Disc rotation leads to the formation of a stable liquid meniscus, facilitating aspiration of the supernatant fluid into a downstream chamber. This step is achieved by a capillary valve at the bottom of the chamber that opens at a specific and adjustable rotation threshold, thus enabling sequential washing and elution steps.

The axial position of the magnetic ring is then adjusted to remove the magnetic field from the beads, allowing them to be re-suspended in the wash buffer through the shaking mode. This iterative collection and release process, controlled by the rotational speed and axial positioning of the magnetic ring, provides a high degree of control over bead handling and ensures effective sample processing for an immunoassay performed within the setup.

2.2 Disc design

The disc design consists of two primary chambers: an upper chamber (collection chamber) and a downstream chamber (waste chamber, see Fig. 2B), connected by a narrow microchannel. This 100 μm wide microchannel with a height of 70 μm effectively controls fluid flow between the chambers. The interruption of the microchannel acts as a capillary valve. This capillary valve is critical for staged fluid transfer and enables precise fluid handling during the washing and elution phases. The capillary valve passively controls fluid flow by balancing centrifugal and capillary forces at the interface between the microchannel and the valve. The valve holds the fluid in place until the rotational speed increases to the point where the centrifugal force overcomes the capillary force, causing the fluid to burst. This threshold is called the burst frequency.[24] The disc arrangement is shown in Fig. 2B.

2.3 Disc fabrication

The disc is fabricated by stacking laser-cut polymethyl methacrylate (PMMA) sheets with cutter-plotted pressure-sensitive

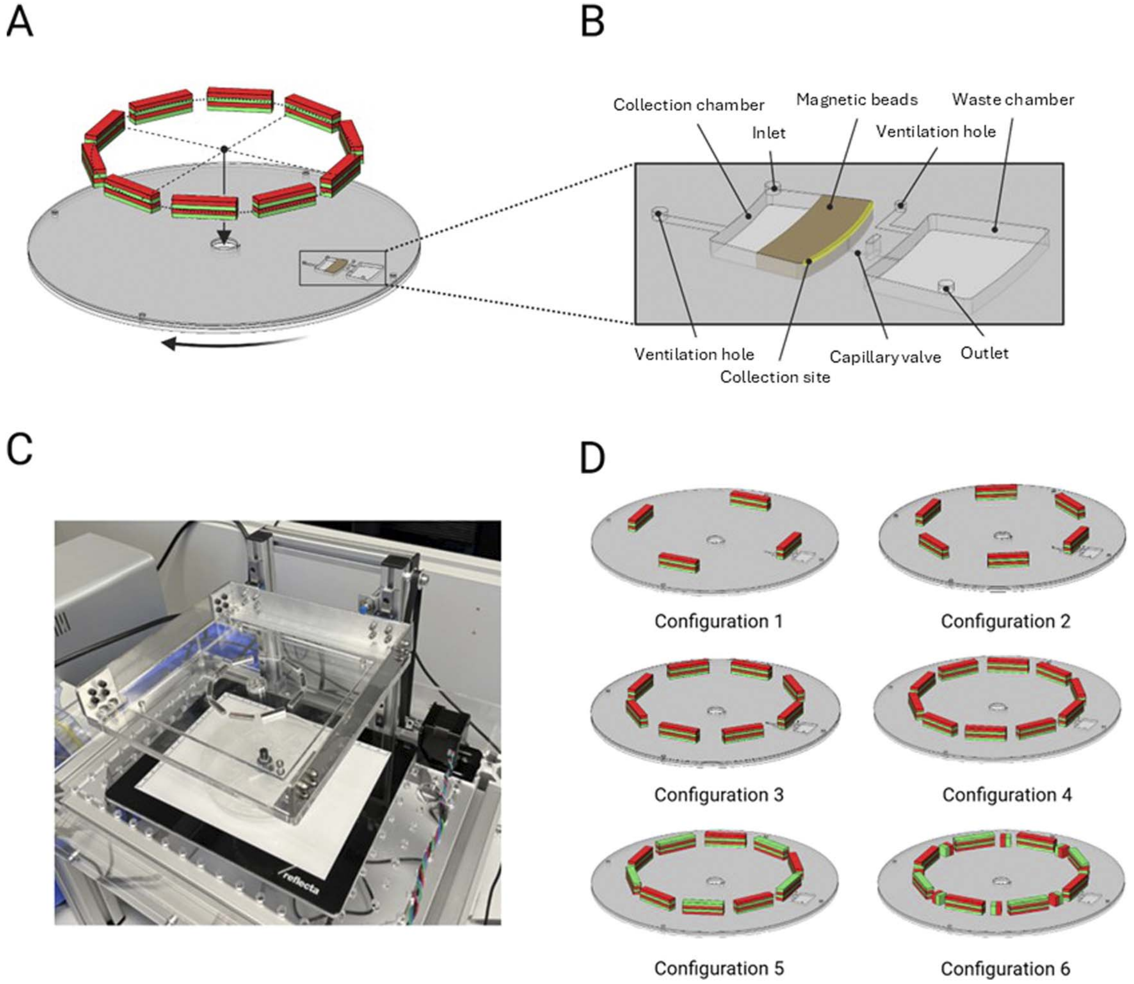

Fig. 2 Magnetic beads collection setup. (A) By controlling the axial position of the permanent magnet ring, magnetic bead collection can be switched on and off. The radial position of the permanent magnets is fixed and corresponds to the outer edge of the collection chamber, which is also the collection site of the magnetic beads. (B) The disc design consists of an upper chamber (collection chamber), a capillary valve, and a downstream chamber (waste chamber). The upper chamber contains a filling hole (inlet) for liquid input and a microchannel to a venting hole (ventilation hole). The downstream chamber also contains a microchannel to a venting hole and an outlet hole for liquid removal. The collection site (yellow line) is shown at the top of the collection chamber. (C) Image of the test rig. (D) Studied permanent magnet configurations.

adhesive (PSA) layers. It consists of five primary layers: a PMMA base layer for structural stability (1.5 mm thickness), a PSA layer with microchannels to control fluid flow, a PMMA layer forming the upper and lower chambers (1 mm thickness), a PSA layer connecting the venting holes, and a PMMA layer with venting holes for pressure regulation (0.5 mm thick). Each layer ensures structural integrity, fluid containment, and reproducibility. PSA layers seal the PMMA sheets, prevent fluid leaks, and precisely align the microfluidic channels. The layered structure of the disc is shown in Fig. S1 of the SI.[25–27]

2.4 Design of the lab-on-a-disc device for the analysis of magnetophoretic bead collection

The experimental setup and the entire device are shown in Fig. 2C. The device enables precise control of disc rotation, permanent magnet positioning, and image acquisition for the analysis of the bead behavior. It includes a BLDC motor controlled by a Nanotec driver and an Arduino microcontroller, allowing adjustable rotational speeds. A Python-based GUI enables intuitive control and monitoring of system parameters.

Illumination is provided by a light pad beneath the disc, ensuring uniform illumination. A camera above the disc captures real-time images, synchronized to the disc's rotation. An optical sensor detects a reflective tape mark, creating a stroboscopic effect. This allows the bead movement to be tracked with a typical spatial and temporal resolution of 17.6 µm and 0.12 s (for 500 rpm), respectively.

The permanent magnet array is mounted on a linear axis with a stepper motor-driven timing belt for controlled vertical movement. The displacement of the ring from the upper to the lower position, *i.e.*, switching the applied magnetic field from near zero to its maximum value, takes 1 s. The magnets are embedded in a transparent acrylic holder, allowing optical monitoring while maintaining magnetic field alignment.

2.5 Permanent magnet configurations

Six configurations of permanent magnets were tested to analyze the influence of the magnetic field on the magnetic bead collection, as shown in Fig. 2D. These configurations were chosen to cover a representative range of magnetic conditions that are commonly encountered in centrifugal platforms. Furthermore, practical design criteria have been considered, including compatibility with our experimental holder and the ability to span a broad range of field magnitudes at the collection chamber. More precisely, we use:

- Configuration 1: four pairs of 20 mm × 4 mm × 3 mm N48 neodymium magnets, stacked vertically and equally positioned in a circular manner (weak field magnitude).
- Configuration 2: six pairs of vertically stacked N48 magnets, equally positioned (intermediate field magnitude).
- Configuration 3: eight pairs of vertically stacked N48 magnets, equally positioned (intermediate field magnitude).
- Configuration 4: ten pairs of vertically stacked N48 magnets, equally positioned (strong field magnitude).
- Configuration 5: ten pairs of N48 magnet stacks with alternating pole orientation to increase the magnetic flux gradient.
- Configuration 6: eight pairs of 5 mm N45 cube magnet and N48 stacks with alternating poles, horizontally interspersed, creating a concentrated unidirectional magnetic field using a so-called Halbach configuration.

Note that the permanent magnets used, N48 or N45, were chosen as commercially available and cost-effective magnets showing reasonable remanence flux density and polarization in the direction of the shortest edge. Further, their geometric dimensions enable us to place them along the ring with appropriate orientation to the disc. Importantly, our model is not restricted to the use of N45 or N48. To facilitate the transposition of our results to other systems, we provide the magnetic flux densities in the collection chamber for all configurations in the SI. Associated slip velocities are also displayed for completeness (Fig. S6).

Simulations were performed for all six configurations using different distances to the disc: 2 mm, 4 mm, and 6 mm to further assess the effects of magnet ring-to-disc distance on magnetophoretic speeds in the collection chamber. Magnetic flux densities and associated slip velocities are shown in (Fig. S7) of the SI.

3 Experimental validation

3.1 Experiments to assess the collection speed and to validate the model simulations

Using the experimental setup described in Section 2, bead collection fractions were measured experimentally in the collection chamber and used to validate the predictions of the multiphysics simulation model. The bead collection process was recorded with a temporal resolution of 0.12 s with a camera mounted above the system (see Fig. 3A). We used the permanent magnet configuration 1 in Fig. 2, with the magnets positioned 2 mm above the liquid surface. The disc rotation speed was set to 500 rpm. A water-diluted Dynabeads M270 solution (60 µl, 1g l^{-1}) was used.[28] The magnets were positioned so that they did not interfere with the camera frames. The camera was positioned to maximize resolution, and the disc was uniformly illuminated from below. Using the Beer–Lambert Law and a calibration curve, the bead concentration was determined from the image pixel intensities.[29,30] The calibration curve, generated from recorded images of the bead solutions (0g l^{-1} to 1g l^{-1} in 0.1g l^{-1} steps), showed a strong correlation (R^2 = 0.9975), validating the use of pixel intensities for concentration calculation. The disc with the bead dilutions and the generated concentration curve are shown in Fig S2 and S3 of the SI, respectively.

Based on the calibration curves, the fraction of beads collected in the collection area (see Fig. 3A) was determined by

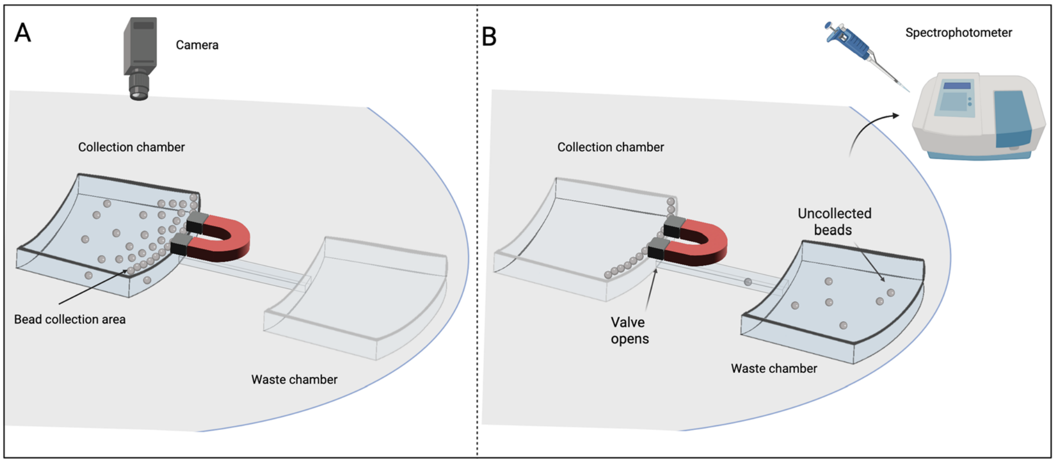

Fig. 3 Experimental setup for the assessment of bead concentrations. (A) A camera above the disc captures real-time images of the collection chamber using magnet Configuration 1. The bead concentration is determined from the pixel intensities of the camera images using a calibration curve. (B) The reliability of the bead collection during supernatant aspiration is determined from absorbance measurements of the supernatant taken from the waste chamber after opening of the valve using the best performing magnet Configuration 5. Created in BioRender. Rienmüller T. (2026) https://BioRender.com/pjtkkf8.

quantifying how many beads remained outside the magnetic bead collection area. For this purpose, the collection chamber was analyzed, excluding a 1 mm strip along the outer radius, which represents the region where the beads ultimately accumulate at the magnet. Beads detected in the remaining area therefore correspond to beads that have not yet been collected. A frame recorded after 120 seconds showed that the bead accumulation did not exceed 1 mm in thickness.

The bead collection fraction $\beta_{\text{i,exp}}$ determined with this imaging method is defined as

$$\beta_{i,\text{exp}} = 1 - \frac{\sum \log(I_\text{e}/I)}{A_\text{roi} \log(I_\text{e}/I)} \tag{1}$$

where I denotes the pixel intensities of the camera images, I_0 the initial intensity of the bead solution, and I_e the final intensity of the cleared water, the number of pixels in the region of interest is denoted by A_roi. Intensity values range from 0 to 255. The same quantity was calculated in the simulation and later on declared as $\beta_{\text{i,sim}}$.

3.2 Experiments for collection reliability and reproducibility

The best performing magnet configuration, Configuration 5, at a distance of 2 mm, was used to assess the reliability of magnetic bead collection during supernatant aspiration into the waste chamber (see Fig. 3B). A disc with 20 collection chambers was designed to perform 20 collection processes simultaneously. In this experiment, the collection efficiency is determined by analyzing the supernatant from each of the 20 parallel processes after opening the capillary valve at the bottom of the collection chambers. Each collection chamber was loaded with 60 μl of Dynabeads M270 (1g l^{-1}). The magnetic bead collection process began with a disc rotating at 500 rpm and the permanent magnet ring in the bottom-most position, right above the disc. After 10 seconds of bead collection, the rotational speed was increased to 4000 rpm, opening the capillary valve and aspirating the supernatant into the downstream waste chamber. The high rotational speed ensured rapid aspiration, thus preventing prolonged collection time. The centrifugal force pushed the remaining beads into the supernatant against the outer wall of the waste chamber. A shaking procedure was then used to homogeneously distribute the beads in the supernatant for subsequent measurements.

In these experiments, the bead concentration in the waste chamber was much smaller than in the previous experiments. Thus, the bead concentration in the waste chamber was determined by measuring the absorbance spectrum of the supernatant at 700 nm, where the beads exhibit their maximum absorption using a Shimadzu UV-2101PC Spectrophotometer. Again, a calibration curve was created by measuring the absorbance spectra of known bead concentrations, which confirmed a strong linear relationship ($R^2 = 0.99$). This validated the use of absorbance for concentration calculation.

The collection fraction β_a determined using this absorbance-based method was defined as the percentage of beads collected from the initial solution and was calculated as

$$\beta_\text{a} = 1 - \frac{c_\text{s}}{c_0} \tag{2}$$

where c_s denotes the concentration of the supernatant and c_0 denotes the initial concentration.

4 Mathematical modeling of magnetophoresis

The collection of magnetic beads in the collection chamber was simulated using COMSOL Multiphysics version 6.3, together with the microfluidics module, the ACDC module and the CAD module. The simulation combined the magnetic field of the permanent magnet, the changing magnetic field due to the disc's rotation, centrifugal forces, and fluid dynamics. The solution was modeled as a single phase with the physical properties of water (viscosity η of 1 mPas, density ρ_fluid of 1000 kg m^{-3}). The beads were spherical particles with a radius R of 1.4 μm, a density ρ of 1600 kg m^{-3}, and an initial concentration of 1g l^{-1}.[28]

To simplify the simulation and avoid computationally intensive time-dependent rotational movement and remeshing, the model calculates an average magnetic force over a complete rotation cycle. This is justified by the fact that the time scales of the primary forces acting on the beads (magnetophoretic motion, centrifugal forces) are much slower than the duration required for one disk rotation, as described below.

The particle slip or drift velocity induced by magnetophoresic effects only, v_mag, can reach approximately 10^{-3} m s^{-1}, with a characteristic length scale L of 10^{-3} m. Thus, the time scale for magnetophoretic motion, T_mag, is

$$T_\text{mag} = \frac{L}{v_\text{mag}} \approx 1 \text{ s}$$

With a rotational frequency f of 10 Hz, the rotational period T_rot is

$$T_\text{rot} = \frac{1}{f} \approx 0.1 \text{ s}$$

The particle slip or drift velocity induced by centrifugal acceleration only, v_cent, which drives the beads towards the chamber wall, is also in the order of 10^{-3} m s^{-1}. The corresponding centrifugal drift time scale T_cent is

$$T_\text{cent} = \frac{L}{v_\text{cent}} = \frac{L}{v_\text{cent}} \approx 1 \text{ s}$$

Since T_rot (0.1 s) is much shorter than T_mag (1 s) and T_cent (1 s), the disc completes multiple rotations before significant magnetophoretic or centrifugal particle drift occurs.

4.1 Modeling the prevailing forces

The movement of magnetic beads in a liquid is governed by magnetic forces, viscous drag, effective body forces arising from gravity or centrifugal acceleration (corrected for buoyancy), inter-particle interactions such as chain formation and agglomeration, magnetophoresis-induced convection, and Brownian motion, as schematically illustrated in Fig. 4. A

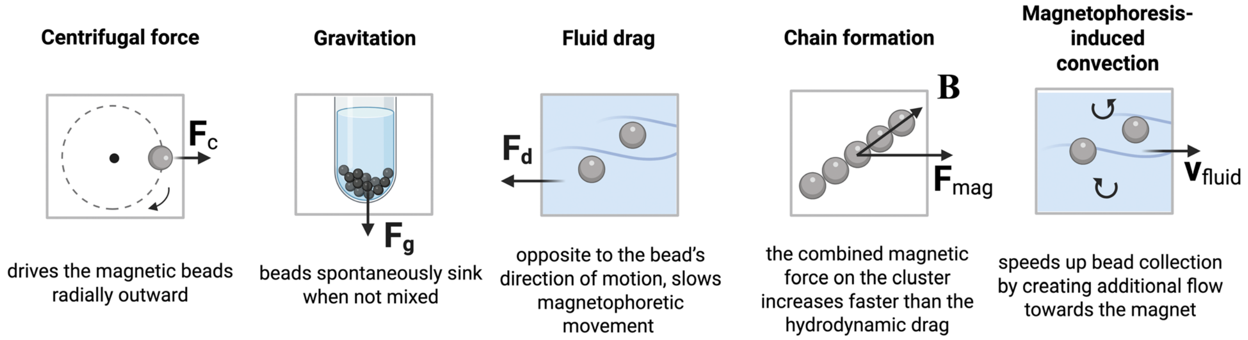

Fig. 4 Schematic of the physical mechanisms governing magnetic bead behavior in a lab-on-a-disc chamber. Bead motion is determined by magnetic forces (F_{mag}), viscous drag (F_d), and effective centrifugal body forces corrected for buoyancy (F_c). Inter-particle attractions lead to chain formation, while magnetophoresis-induced convection, represented by the fluid velocity field (v_{fluid}), further influences bead transport and accumulation. Brownian motion is not shown explicitly, as it primarily facilitates short-range bead–bead encounters contributing to chain formation. Created in BioRender. Rienmüller T. (2026) https://BioRender.com/kv1ipmg.

Eulerian approach is used to describe the concentration field using the advection–diffusion equation. From these forces, the velocity of the magnetic beads is then calculated and inserted into the advection–diffusion equation.[31]

The collection of magnetic beads is based on a magnetic flux density gradient. Under an external magnetic flux density, a torque acts on the bead's magnetic dipole, aligning it with the flux density. The bead's movement direction is determined by the gradient of the magnetic flux density. A permanent magnet generates a magnetic flux density with strong values near the magnet and low values farther away, creating a gradient toward the magnet. This causes the beads to migrate toward the magnet.[32–35]

The primary force acting on a bead during magnetophoresis is the magnetic force $\mathbf{F}_{\text{mag}}$. For a single magnetic bead, $\mathbf{F}_{\text{mag}}$ on the dipole moment m can be calculated as[36,37]

$$F_{\text{mag}} = \frac{m_{\text{sat}}\mathscr{L}(|\mathbf{B}|)}{|\mathbf{B}|}(\mathbf{B}\cdot\nabla)\mathbf{B}, \tag{3}$$

where $\mathbf{B}$ is the magnetic field, $|\mathbf{B}|$ is the magnetic flux density and $m_{\text{sat}} = \rho(4R^3\pi/3)M_{\text{sat}}w$ is the saturation dipole moment. Measurements[38] yield a saturation magnetization M_{sat} of 6.4 Am^2/kg and an iron content w of 14% for the M-270 beads. The magnetization curve is derived from the Langevin function $\mathscr{L}(\alpha|\mathbf{B}|) = \coth(\alpha|\mathbf{B}|) - (\alpha|\mathbf{B}|)^{-1}$ with the Langevin parameter α. By examining the magnetization curve of the M-270 beads, α could be estimated as 53T^{-1}.[36,39] A more detailed description of the Langevin curve and a representation of the magnetization curve of Dynabeads M270 can be found in Fig. S4 of the SI.

The drag force $\mathbf{F}_{\text{d}}$ on a magnetic bead suspended in a liquid and subjected to Stokes flow (Reynolds number <1) is given by

$$\mathbf{F}_{\text{d}} = -6\pi\eta R\mathbf{v}_{\text{slip}} \tag{4}$$

This takes into account the relative velocity of a magnetic bead to the fluid, also known as the resulting slip velocity $\mathbf{v}_{\text{slip}}$, which is typically in the range of 50 μm s^{-1} to 500 μm s^{-1} for the collection of target analytes in microfluidic chambers.[38,39]

The gravitational force F_{g} acting on a bead in combination with the buoyancy can be calculated as

$$\mathbf{F}_{\text{g}} = (\rho - \rho_{\text{fluid}})\frac{4R^3\pi}{3}g \tag{5}$$

which roughly corresponds to 7×10^{-14} N. Here, $\mathbf{g}$ is the gravitational acceleration.[18]

The centrifugal force $\mathbf{F}_{\text{c}}$, depending on the mass of the bead, the angular velocity ω and the distance to the rotational axis in x-direction and y-direction (with unit vectors $\hat{\mathbf{e}}_x$ **and** $\hat{\mathbf{e}}_y$ respectively), is given by[40]

$$\mathbf{F}_{\text{c}} = \frac{4R^3\pi}{3}(\rho - \rho_{\text{fluid}})\omega^2(x\hat{\mathbf{e}}_x + y\hat{\mathbf{e}}_y), \tag{6}$$

which is about 7×10^{-13} N at 500 rpm.

Other phenomena influencing bead motion are cooperative movement and magnetophoresis-induced convection, which lead to an increase in the bead collection speed and are included in the modeling process, see Sections 4.2 and 4.3.

4.2 Cooperative movement of magnetic beads

Cooperative movement describes the increased migration velocity of agglomerated magnetic bead clusters compared to individual beads. This phenomenon increases with increasing bead concentrations in the solution. Magnetic beads tend to form chains rather than random patterns due to the interaction energy between superparamagnetic particles. The anisotropy of this energy leads to repulsion perpendicular to the dipole direction and attraction along the dipole moment, which favors chain formation.[14] Chain formation results in faster movement of the bead clusters due to a higher magnetic dipole moment and a stronger magnetic force. Although drag resistance increases, this remains a second-order effect.[20]

The aggregation parameter N^* determines whether a cooperative movement takes place and is calculated as

$$N^* = \sqrt{\Phi_0\, e^{\Gamma-1}} \tag{7}$$

where Φ_0 is the initial volume fraction and Γ is the coupling parameter. Values above 1 indicate cooperative motion, while values below 1 suggest that the beads move in isolation from each other.

The coupling parameter Γ describes the ratio of magnetic to thermal energy and is determined as

$$\Gamma = \frac{\mu_0 m^2}{16\pi R^3 kT}, \tag{8}$$

where μ_0 is the magnetic permeability in vacuum, m is the magnetic moment of the particle, k is the Boltzmann constant, and T is the absolute temperature. With the magnetic beads used and the magnetic field applied in the setup, Γ is 3.1×10^4, *i.e.*, N^* is significantly higher than 1, which indicates cooperative movement.[14] High Γ values lead to high chain lengths under equilibrium conditions. However, equilibrium cannot be reached on the time scale of the process, so the problem must be treated as a sequence of non-equilibrium states, with the average number of beads in a chain $N(t)$ growing with time according to the power law

$$N(t) \approx \left(\frac{t}{t_{\mathrm{BW}}}\right)^{1/2}, \tag{9}$$

where t_{BW} denotes the characteristic time scale, which physically represents the mean time required for two initially separated particles to encounter each other due to Brownian motion (and which is modified by attractive dipolar interactions), given by[41]

$$t_{\mathrm{BW}} = \frac{9.16R^2}{6D\Phi^{4/3}}, \tag{10}$$

where Φ is the volume fraction, which in turn depends on time.

To implement chain growth in COMSOL Multiphysics®, the time derivative of eqn (9) is used, limited by a minimum growth rate of 0. This results in

$$\frac{D}{D_t}N(t) = \max\left[\left(\frac{18.32R^2}{3D\Phi\Gamma^{4/3}}\right)^{-1/2}\frac{\left(\Phi + \dot{\Phi}_t\right)}{(\Phi_t)^{1/2}}, 0\right] + \mathbf{v}_{\mathrm{p}}\cdot\nabla N, \tag{11}$$

where $\mathbf{v}_{\mathrm{p}}$ is the local particle velocity, and thus, also the local bead chain velocity relative to the chamber. The term $\mathbf{v}_{\mathrm{p}}\cdot\nabla N$ accounts for the advection of the chain length field N as the chains are transported at v_{p} through the chamber.

After calculating the chain length, the hydrodynamic drag and the magnetic force acting on the bead chains can be determined. The magnetic field direction at any point in space provides the direction vector $\mathbf{e_B} = \mathbf{B}/|\mathbf{B}|$ for further calculations. The magnetic, centrifugal, and gravitational forces acting on a single bead are summed and multiplied by the average number of beads in a chain to obtain the resulting force $\mathbf{F}_{\mathrm{Res}}$ on the aggregate, *i.e.*,

$$\mathbf{F}_{\mathrm{Res}} = N(\mathbf{F}_{\mathrm{mag}} + \mathbf{F}_{\mathrm{g}} + \mathbf{F}_{\mathrm{c}}). \tag{12}$$

The resulting force $\mathbf{F}_{\mathrm{Res}}$ is projected onto the direction of the magnetic field and results in

$$\mathbf{F}_{\mathrm{Res}\parallel} = (\mathbf{F}_{\mathrm{Res}}\cdot\mathbf{e}_{\mathrm{B}})\,\mathbf{e}_{\mathrm{B}} \tag{13}$$

The perpendicular component $\mathbf{F}_{\mathrm{Res}\perp}$ is then calculated as

$$\mathbf{F}_{\mathrm{Res}\perp} = \mathbf{F}_{\mathrm{Res}} - \mathbf{F}_{\mathrm{Res}\parallel}. \tag{14}$$

To go further, we assume that the chain can be modeled as an ellipsoid. The drag force on an ellipsoidal aggregate is divided into parallel and perpendicular components, with the orientation relative to the principal axis of the ellipsoid. Using Newton's second law, this gives

$$-\mathbf{F}_{\mathrm{d}\parallel} = \mathbf{F}_{\mathrm{Res}\parallel} = 6\pi\eta\ R_{\mathrm{eff}}\, f_{\parallel}\mathbf{v}_{\mathrm{slip}\parallel}, \tag{15}$$

$$-\mathbf{F}_{d\perp} = \mathbf{F}_{\mathrm{Res}\perp} = 6\pi\eta\ R_{\mathrm{eff}}\, f_{\perp}\ \mathbf{v}_{\mathrm{slip}\perp}, \tag{16}$$

which allows determination of the particle slip velocity in the direction of the magnetic field $\mathbf{v}_{\mathrm{slip}\parallel}$ and perpendicular to it $\mathbf{v}_{\mathrm{slip}\perp}$. The factors $f_{\parallel}$ and $f_{\perp}$ are the Stokes correction factors, defined as the ratio of the drag forces acting on a spheroid to those acting on a sphere of the same volume. The effective radius R_{eff} is defined with the help of the bead radius R and ellipsoidal aspect ratio E, approximated here by N, the number of beads in a chain. It provides

$$R_{\mathrm{eff}} = RE^{1/3} = RN^{1/3} \tag{17}$$

The Stokes correction factors can then be calculated as[42]

$$f_{\parallel} = \frac{(4/3)E^{-1/3}\left(1 - E^2\right)}{E - \dfrac{\left(2E^2 - 1\right)\ln\left(E + \sqrt{E^2 - 1}\right)}{\sqrt{E^2 - 1}}}, \tag{18}$$

$$f_{\perp} = \frac{(8/3)E^{-1/3}\left(E^2 - 1\right)}{E + \dfrac{\left(2E^2 - 3\right)\ln\left(E + \sqrt{E^2 - 1}\right)}{\sqrt{E^2 - 1}}}. \tag{19}$$

Finally, the particle slip velocity resulting from magnetic, centrifugal, and drag forces $\mathbf{v}_{\mathrm{slip}}$ is determined by adding the parallel and perpendicular components according to

$$\mathbf{v}_{\mathrm{slip}} = \mathbf{v}_{\mathrm{slip}\parallel} + \mathbf{v}_{\mathrm{slip}\perp}. \tag{20}$$

4.3 Magnetophoresis-induced convection

The second phenomenon that can accelerate magnetophoretic bead collection is magnetically induced convection. When a permanent magnet is placed next to a well containing a magnetic bead suspension, the magnetic field gradient is strongest near the magnet. Beads in this region are therefore attracted and removed from the bulk more rapidly than beads farther away, creating a local depletion zone and a concentration gradient in the suspension. The combination of this concentration inhomogeneity and the spatially varying magnetic body force can drive fluid motion (induced convection) that further accelerates bead transport.[14]

In a suspension, liquid movement influences that of the suspended particles and *vice versa*. To account for these effects, two-way coupling is used. This takes into account not only the friction of the fluid on the particles, but also the momentum transfer from the particles to the fluid, which may lead to magnetophoresis-induced convection. This convection can be modeled using the Navier–Stokes equations, which assume incompressible flow with a Newtonian fluid. The Navier–Stokes equation reads

$$\rho\left(\frac{\partial \mathbf{v}_\mathrm{fluid}}{\partial t} + \left(\mathbf{v}_\mathrm{fluid}\cdot\nabla\right)\mathbf{v}_\mathrm{fluid}\right) = -\nabla p + \nu\nabla^2\mathbf{v}_\mathrm{fluid} + \frac{cN_\mathrm{A}\mathbf{F}_\mathrm{Res}}{N}, \quad (21)$$

where $\mathbf{v}_\mathrm{fluid}$ denotes the fluid velocity vector, p the pressure, ν the kinematic viscosity, c the Eulerian concentration field of the magnetic beads and N_A the Avogadro constant. eqn (21) shows a transient term and a convective term on the left side, and a pressure force term, a viscous force term, and a volumetric force term on the right side. One-way coupling would result in the same equations without including the volumetric force term, *i.e.*, without any influence of the particles on the fluid. This volumetric force term represents the body force density exerted on the fluid by the particle phase, obtained here as the local number density of beads cN_A multiplied by the force per bead $\mathbf{F}_\mathrm{Res}/N$. It increases with increasing concentration of magnetic beads, as more momentum is transferred from the beads to the fluid. The conservation of mass and the assumption of an incompressible fluid result in the continuity equation, which leads to the divergence of the fluid velocity being zero.

When modeling magnetophoresis-induced convection, the previously introduced particle velocity vector $\mathbf{v}_\mathrm{p}$ of the magnetic beads can be calculated as a superposition of the particle slip velocity relative to the fluid obtained from the force-drag balance using the resultant external force $\mathbf{F}_\mathrm{Res}$ from eqn (12) $\mathbf{v}_\mathrm{slip}$ and the fluid velocity vector $\mathbf{v}_\mathrm{fluid}$, reading

$$\mathbf{v}_\mathrm{p} = \mathbf{v}_\mathrm{slip} + \mathbf{v}_\mathrm{fluid}. \quad (22)$$

This velocity $\mathbf{v}_\mathrm{p}$ is used in the convection–diffusion equation to advect the bead concentration field c. The latter enters into the body-force term of the Navier–Stokes equation, leading to magnetically induced convection. More precisely, the concentration field c of magnetic beads is obtained by solving

$$\frac{\partial c}{\partial t} = D\nabla^2 c - \nabla\cdot\left(\mathbf{v}_\mathrm{p}c\right), \quad (23)$$

where D is the bead diffusion coefficient, which determines the diffusion part, and $\mathbf{v}_\mathrm{p}$ the convective part. The diffusion constant in the convection–diffusion eqn (23) can be calculated with the Stokes–Einstein equation using the hydrodynamic radius R of the beads and the dynamic viscosity η of the liquid, providing

$$D = \frac{k_\mathrm{B}T}{6\pi\eta R} \quad (24)$$

where T is the absolute temperature, and k_B is the Boltzmann constant. For the fluid solver, we apply a no-slip boundary condition at the chamber walls, *i.e.*, the fluid velocity is set to zero on the walls.[19]

Magnetic beads move through the fluid until they reach a wall, where they leave the fluid domain and thereby increase the surface density of magnetic beads s. The calculated steady-state particle velocity should therefore remove magnetic beads from the liquid at the boundary if it points outwards, without adding beads to the system if pointing inwards. This concept leads to a boundary condition for the Eulerian concentration field according to

$$\mathbf{n}\cdot\mathbf{j}_\mathrm{bound} = \mathbf{n}\cdot[c\mathbf{v}_\mathrm{p} - D\nabla c]\Theta(\mathbf{n}\cdot\mathbf{v}_\mathrm{p}), \quad (25)$$

where Θ denotes the Heaviside step function, $\mathbf{n}$ denotes the outward normal vector of the boundary wall and $\mathbf{j}_\mathrm{bound}$ denotes the bead flux at the boundary. The factor $\mathbf{n}\cdot\mathbf{v}_\mathrm{p}$ of the Heaviside function enforces an outflow condition only: if positive, then $\Theta = 1$ and the beads leave the domain; if negative, $\Theta = 0$ so that no inward flux is generated.

As the magnetic beads flow out of the fluid domain, they are trapped at the boundary, increasing the surface density of the magnetic beads s, defined at the boundary of the fluid domain. The surface density is zero at the beginning of the bead collection process across the boundary and increases over time as more magnetic beads are trapped. The increase in surface density corresponds to the magnetic bead flux $\mathbf{j}_\mathrm{bound}$, as shown in 25. The following partial differential equation (PDE) can now be used to determine the surface density at any point of the boundary:

$$\frac{\partial s}{\partial t} = \mathbf{n}\cdot\left[c\mathbf{v}_\mathrm{p} - D\nabla_\mathrm{c}\right]\Theta\left(\mathbf{n}\cdot v_\mathrm{p}\right) - \nabla\cdot\left(s\mathbf{v}_\mathrm{p}\right). \quad (26)$$

The last term accounts for the movement of magnetic beads at the boundary, assuming that there is no friction between the beads and the wall.[43]

To determine the collection efficiency in the simulations, the experimental approach is transferred to the numerical results, allowing a direct comparison. First, the initial total number of beads, say $n_\mathrm{beads,0}$, in the region of interest is determined. These are the beads inside the chamber, excluding the outer 1 mm thick region, the bead collection area. Subsequently, three-dimensional bead concentration can be projected onto the *xy*-plane by integration over the *z*-direction, yielding the bead surface density. The latter can be further integrated over the region of interest (*xy*-plane) at each time step and is noted as $n_\mathrm{beads,i}$. These two variables allow the definition of a collection fraction according to

$$\beta_\mathrm{i,sim} = \frac{n_\mathrm{beads,i}}{n_\mathrm{beads,0}}, \quad (27)$$

which is based on the same principle as the experimentally determined collection fraction $\beta_\mathrm{i,exp}$, presented in Section 3.1.

4.4 Finite element simulations

Simulations of the bead collection process were performed using the finite element analysis software COMSOL Multiphysics® version 6.3. The ACDC module was used to simulate the magnetic field, the transport of diluted species module for the Eulerian concentration field, the laminar flow module for the magnetophoresis-induced convection, and a coefficient form boundary PDE for the surface density of magnetic beads. To calculate the mean number of beads in a chain, a coefficient form PDE was used. Note that these values remain local, as they are a function of time and the current concentration at a given point in space. Finally, the diffusion term, initially 1.5×10^{-13} m^2 s^{-1}, was increased by a factor of 5000 to stabilize the simulation, which includes a large convective contribution. The 6 different magnet configurations were simulated at a rotational speed of 500 rpm and a magnet-fluid distance of 2 mm. The rotational speed was varied between 300 and 800 rpm, and the magnet-fluid distance between 2 and 6 mm.

5 Results and discussion

5.1 Phenomena increasing the collection speed and model validity domain

The simulations demonstrated the importance of transport phenomena that enhance the collection speed of magnetic beads within the centrifugal microfluidic platform. Here we distinguish between (i) magnetophoresis-induced convection, *i.e.*, the fluid flow generated by the motion of the beads, and (ii) cooperative bead motion, *i.e.*, the formation and collective migration of bead chains in the magnetic field. Switching off both effects increases the time required to reach a collection fraction of 50% by a factor of 3.875 compared to the full model. The dominant effect arises from cooperative bead motion, while magnetophoresis-induced convection provides an additional, though smaller, reduction of the collection time, see also Fig. S5 of SI presenting the results of a simulation performed without aggregation and/or without two-way coupling.

The magnetophoretic-induced convection developing within the collection process is shown in Fig. 5A. At 0 s, the beads are initially subjected to gravitational, centrifugal, and magnetophoretic forces, which drive them radially toward the collection zone. Because the beads move relative to the surrounding fluid, their slip velocity transfers momentum to the liquid and generates a convective flow. As time progresses, and more beads are accelerated toward the collection zone, the fluid velocities increase due to the continuous influence of this slip. This enhanced convection contributes to the transport of the magnetic beads to the collection site with fluid velocities of $\mathbf{v}_{\text{fluid}} = 1\ \text{mm s}^{-1}$ that are comparable to, or even larger than the slip velocity of the beads, which reaches a maximum of about $\mathbf{v}_{\text{slip}} = 0.17\ \text{mm s}^{-1}$ at the beginning of the collection process. Beyond convection, bead aggregation plays a crucial role in the velocity increase. As the beads move through the system, they aggregate into chains under the influence of the magnetic field, further accelerating the collection process.

Initially, the beads are dispersed and separated from each other, but as the magnetic field is applied and the collection process develops, they aggregate into chains of length N. Fig. 5B shows the minimum and maximum local mean number of beads in a chain over time. The aggregation of the beads increases the collective magnetic force, resulting in stronger magnetophoretic forces. Since the associated increase in drag remains small compared to that of the magnetic force, this effectively leads to an increase in the bead velocity and thus improves collection efficiency. After about 3 s, the first chains of 8 beads form, but much smaller chains are still present in the solution, shown by the minimum chain length of Fig. 5B. After about 10 s, the minimum chain length also reaches saturation with 7 to 8 beads per chain. This saturation is due to the rapid decrease in bead concentration caused by the magnetophoresis process.

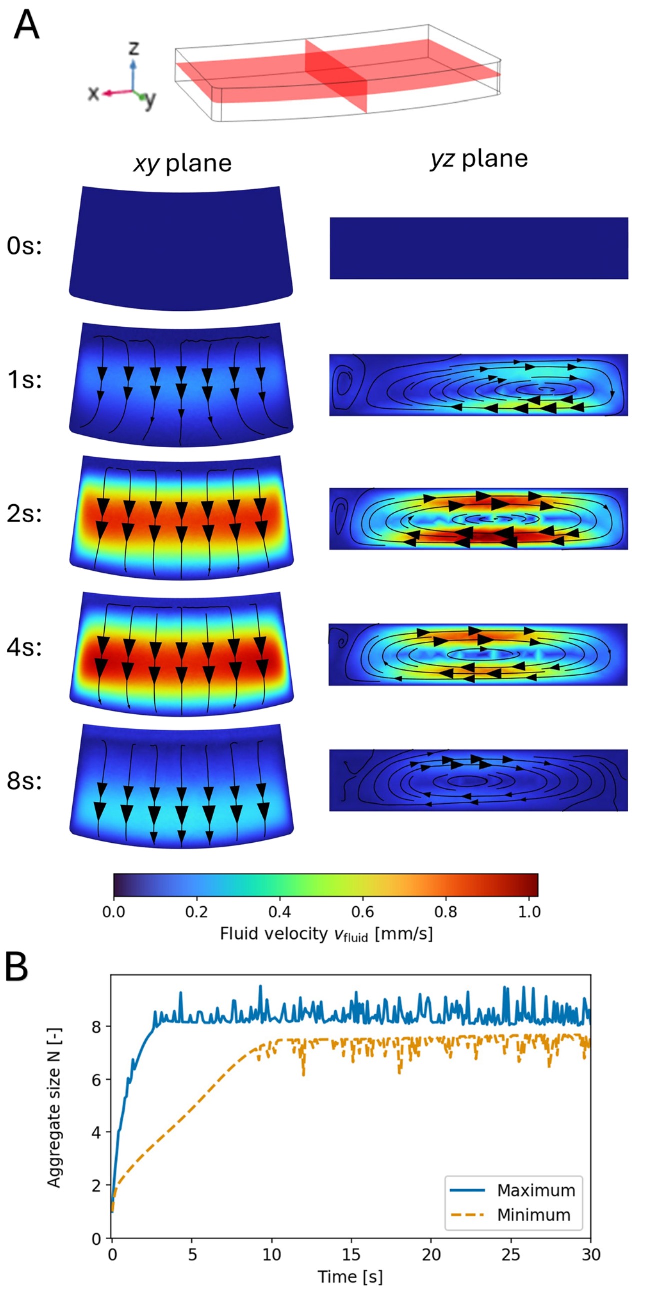

Fig. 5 Bead collection speed enhancement phenomena. (A) Evolution of magnetophoretic-induced convection in the collection chamber along its cross-sections in the *xy*-plane (0.2 mm below the top surface) and the *yz*-plane. The fluid velocity $\mathbf{v}_{\text{fluid}}$ is shown at 0, 1, 2, 4 and 8 s. The flow was simulated with a two-way coupling that incorporated a volumetric term from centrifugal, gravitational, and magnetophoretic force contributions. At the end of the collection process, convection disappears because only a few beads are present in the solution. (B) Minimum and maximum mean number of beads in a chain over time. Bead aggregation increases the effective collection speed, reaching a plateau of 7 to 9 beads per chain after 10 s.

Note that the aggregation process considered in this model only accounts for linear chain growth. Real systems may exhibit cross-linked fiber structures or lateral aggregation, depending on the bead volume fraction and magnetic coupling strength.[41] For the beads and collection process studied here, modeling chains is sufficient and computationally efficient. However, if magnetic coupling is too weak to induce chaining, *e.g.*, for sub-micrometric beads, the aggregation sub-model must be adapted or disabled. Yet, a key advantage of this modeling approach is that it does not require fitting to experimental data, thus providing predictive power and design flexibility without empirical calibration. Indeed, since the model is parameterized by bead radius R, density ρ, and magnetization curve (including the saturation moment m_{sat}), it can be adapted to other bead types. It includes diffusion and assumes inertia-free particle motion (Stokes regime), which is typically valid for micrometric beads.

5.2 Simulation *versus* experiment

To validate the simulation results, a comparison was performed between the simulated and experimentally measured bead concentration fields at different instants (0, 1, 2, 4, 8, and 10 s). The experimental data were obtained from pixel intensities I of the images of the collection chamber, where the bead concentration was determined using the Beer–Lambert law (Section 3.1). The simulation data were obtained by integrating the bead concentration along the z-direction and adding the surface density of beads, making the simulation comparable to the experiments (Section 4.3). Note that the gray scale levels of the simulation were designed to match the gray levels determined for the experimental light absorption, so that both datasets use the same gray levels for the same concentrations. The upper limit of the scale was set to 2 g l^{-1} (1.68×10^{-10} mol m^{-1}), which corresponds to twice the initial concentration, to visualize regions of higher concentration within the collection area. Fig. 6 shows the concentration maps from simulations and experiments. Both the simulations and the experimental measurements show similar distributions and evidence of increasing concentrations near the collection region over time. This suggests that the simulations accurately reproduce the physical behavior of bead transport in the system. Furthermore, the good agreement of the observed gray levels across the entire region of interest shows the quantitative accuracy of our model. A slight difference near the collection area is visible, with a wider and smoother transition for the simulations. This can be well explained by the artificial increase in the diffusion term, which tends to homogenize the bead distribution.

To facilitate the quantitative comparison of simulation and experiment, three areas of 10 pixel × 10 pixel were selected for which the temporal evolution of the bead concentration was tracked, see Fig. 7A. The evolution of the experimental and simulated concentrations at these three points is plotted over 30 seconds. As can be seen, the results for all three areas are in good agreement. Small deviations are observed, which can be explained by some of the model assumptions. First, it is noticeable that the concentrations predicted by the simulations are slightly higher than those measured experimentally for short time periods, typically below 10 seconds. This could be due to increased diffusion, which counteracts the concentration gradient and the absorption of the beads. After longer periods, such as 20 seconds, the simulations show a concentration of zero beads per square meter, while the experimental values remain measurable at approximately 0.05 mol m^{-3}. This could be caused by the idealized collection process of the simulation, which assumes that once a bead leaves the domain, it is irreversibly trapped. In reality, however, it cannot be ruled out that some beads bounce off the wall or are re-dispersed by subsequent incoming beads or strong flows. Thus, it is not surprising that the experimental values do not reach zero as easily as predicted.

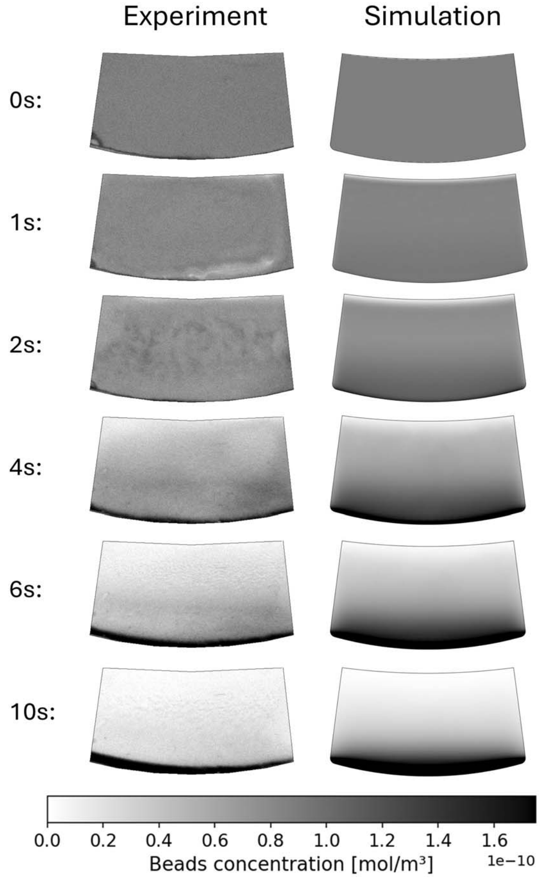

Fig. 6 Bead concentration fields at different times for experiments and simulations. The bead concentration fields in the experiments were determined from the pixel intensities I of the camera image using a calibration curve.

For application purposes, the overall collection fraction is more relevant. Therefore, it is presented in Fig. 7B for both experimental and numerical results. For this purpose, the predicted particle concentration in moles per square meter was integrated across the entire collection chamber, excluding the collection area. Both datasets demonstrate similar collection trends, with the system reaching collection of 90% within a comparable time frame of 13.7 s (simulation) and 15.7 s (experiment). The comparison of the collection fractions between the simulation and experiment shows good agreement and confirms that the simulations provide a physical system. Small deviations can be observed in the long-term local results of Fig. 7A. For $t > 25$ s, the simulated collection fraction reaches the ideal value of 1.0, which is not observed experimentally. As

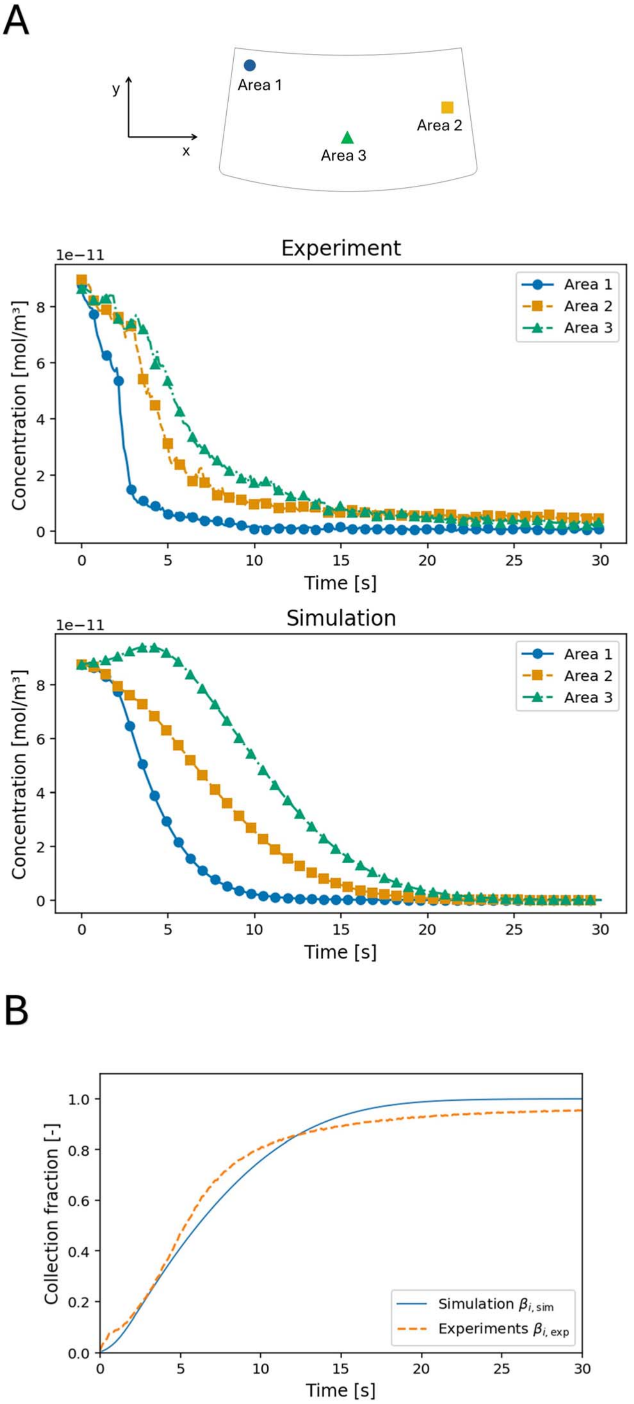

Fig. 7 Quantitative collection results. (A) Bead concentrations at three different points in the collection chamber for simulations and experiments. The bead concentration in the experiments was determined based on the pixel intensities *I* of the camera image at the respective locations. (B) Comparison of collection fractions over time between simulations, $\beta_{i,\mathrm{sim}}$, and experiments, $\beta_{i,\mathrm{exp}}$, for permanent magnet Configuration 1. The simulation and experimental results show similar trends, reaching the 90% collection fraction at similar times, which is 13.7 s for the simulation and 15.7 s for the experiment.

mentioned above, potential bouncing, sliding, and re-dispersion of the beads are to be expected in real systems, but these phenomena were not considered in the present simulations as it goes beyond the scope of our work. Furthermore, the simulation considers a mean number of beads in a chain, whereas in reality, individual beads can remain migrating at significantly lower speeds. Small differences between 5 and 10 seconds could be partly due to the increased diffusion, which tends to slow the collection process. It must also be noted that the model relies on the assumption that chain growth follows a power law, which is valid for magnetic bead aggregation in a non-equilibrium state. While the superparamagnetic microparticles commonly used in practice typically exhibit a high coupling parameter and therefore form chains under non-equilibrium conditions, smaller superparamagnetic nanoparticles may instead reach equilibrium-limited chain lengths. In this case and as already mentioned, other formulations for the chain growth must be used.

5.3 Permanent magnet configurations and simulation parameters

With the validated simulation, it becomes possible to analyze the collection fraction under various permanent magnet configurations and other parameters, such as the disc's rotational speed. This enables the identification of an optimal configuration and parameter set that maximizes the collection fraction, $\beta_{\mathrm{i,sim}}$, within a given time frame. Furthermore, the approach provides deeper insights into the system's sensitivity to specific parameters. Fig. 8 shows the time periods during which each permanent magnet configuration and simulation parameter set achieved the collection $\beta_{\mathrm{i,sim}}$ of 20%, 50%, 80%, 90%, and 95%, respectively. Despite substantial differences in absolute collection times, the overall evolution of the collection process is remarkably consistent across configurations. Differences observed at one threshold (*e.g.*, $\beta_{\mathrm{i,sim}} = 50\%$) closely mirror those at other thresholds (from $\beta_{\mathrm{i,sim}} = 20\%$ up to $\beta_{\mathrm{i,sim}} = 95\%$), with their magnitude increasing over time. This behavior indicates that evaluating a single representative threshold, such as $\beta_{\mathrm{i,sim}} = 80\%$, is sufficient for optimizing the magnet configuration.

We first performed simulations using magnet Configuration 1 placed at 2 mm from the fluid, focusing on the disc's rotational speed, as illustrated in Fig. 8A. As expected, higher rotational speeds generate greater centrifugal forces on the magnetic beads, thereby increasing their radial velocity and shortening the time required for collection. This trend is evident from the times required to achieve 95% collection: 22 s at 300 rpm compared to 12 s at 800 rpm. Within the investigated range, the characteristic collection time t_{c} for high collection fractions (80 to 95%) decreases exponentially with the rotational speed and can be described by an empirical relation of the form $t_{\mathrm{c}}\,(\mathrm{rpm}) \propto \exp\,(-1.24\ 10^{-3}\ \mathrm{rpm})$ offering a good design rule for selecting the rotation protocol in this regime. In the experiments, a rotational speed of 500 rpm was employed as a compromise between rapid bead collection and robust fluidic control, since higher speeds may lead to premature and undesired opening of the capillary valve.

Further, we investigated the influence of the distance between the permanent-magnet ring and the fluid in the

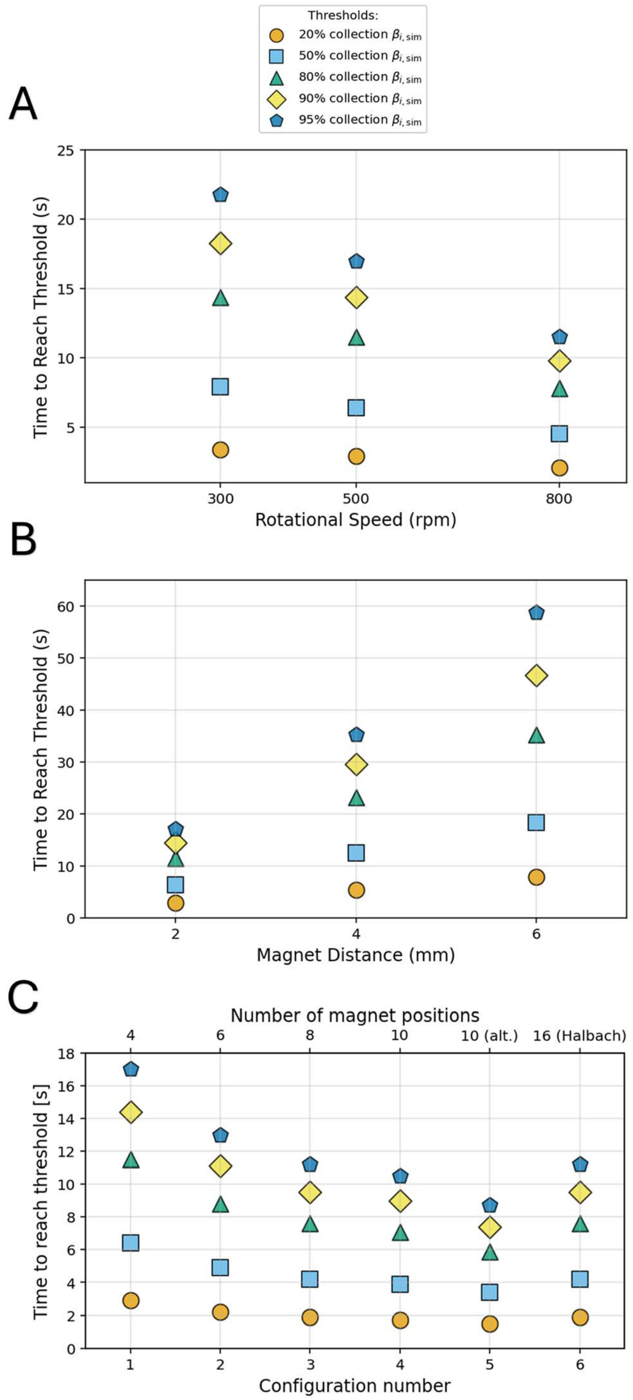

Fig. 8 Simulated times required to reach specified bead-collection fractions $\beta_{\mathrm{i,sim}}$ as a function of (A) magnet–disc distance for Configuration 1 under 500 rpm, (B) rotational speed for Configuration 1 and disc-fluid distance of 2 mm (C) permanent-magnet configuration with disc-fluid distance of 2 mm and 500 rpm. Circles, squares, triangles, diamonds, and pentagons for collection times of 20, 50, 80, 90, and 95%, respectively.

collection chamber along the z-direction, to assess how critical it is to position the magnets close to the disc. Simulations were conducted for magnet Configuration 1 under 500 rpm with magnet–disc distances of 2 mm, 4 mm, and 6 mm, which resulted in times to reach $\beta_{i,\mathrm{sim}} = 95\%$ collection of 17 s, 35 s, and 59 s, respectively (Fig. 8A). These results highlight the strong impact of minimizing the magnet-fluid gap on collection performance. Within the investigated range, the time required to reach a given collection fraction increases approximately linearly with the magnet–disc distance, providing a simple design rule for selecting the magnet position. As a consequence, increasing the distance from 2 mm to 6 mm more than triples the time needed to achieve a targeted collection fraction.

Finally, six different permanent magnet configurations were selected (see Section 2.5) and their effectiveness on bead collection process was assessed by simulations using a 2 mm gap and 500 rpm, see Fig. 8C. Configuration 5 demonstrated the best performance, achieving a 95% collection fraction in the shortest time. This configuration provides optimal placement and magnetic field orientation, resulting in stronger magnetophoretic forces and more efficient bead transport. The results further show that increasing the number of permanent magnets in the ring improves the collection time, and that an alternating-pole arrangement, as used in Configuration 5, yields a pronounced acceleration of the collection process, reaching 95% collection in approximately 9 s.

5.4 Reliability of the collection process

To evaluate the repeatability and reliability of the system, experiments were performed using the best-performing magnet configuration (Configuration 5) at a distance of 2 mm above the fluid. With a rotational speed of 500 rpm. A total of 20 collection processes were analyzed on a single rotating disc as depicted in Fig. 3B. The results obtained on these 20 simultaneous tests show a very high repeatability, with a mean bead collection fraction of $\beta_{\mathrm{a}} = 98\%$ and a standard deviation of 3%. This demonstrates the high reproducibility and reliability of the system and confirms that the centrifugal microfluidic platform with collection parameters and design achieves extremely fast and consistent bead collection.

6 Conclusion

This work presents a quantitative analysis of magnetophoretic bead collection dynamics on centrifugal microfluidic platforms, with a focus on the physical mechanisms and operating parameters that govern bead collection speed. By combining mathematical modeling, numerical simulation, and experimental validation, we show how magnetic forces, centrifugal effects, viscous drag, inter-particle interactions, and magnetophoresis-induced convection jointly determine bead transport and accumulation in rotating lab-on-a-disc chambers.

The developed simulation model accurately predicts the bead transport dynamics, including effects often neglected in simplified models, such as magnetophoresis-induced convection and bead aggregation into chains. The agreement between simulations and experiments is high: both achieve 90% collection within 13.7 s (simulation) and 15.7 s (experiment), confirming the predictive capability of the model. Although real-world aggregation may involve more complex structures, the chain model used here provides sufficient detail to capture the fast collection times.

Within the investigated combinations, the shortest time required to collect 95% is obtained with the magnet Configuration 5, a magnet-disc gap of 2 mm, and a rotational speed of 500 rpm. This collection time lies below 10 s. For this configuration, a collection fraction of $\beta_a > 98\%$ with a standard deviation of only 3% across 20 parallel processes is achieved within 10 seconds in the experiments, highlighting both efficiency and reproducibility. Our results further show that increasing the rotational speed from 300 rpm to 800 rpm systematically decreases the time required to collect a targeted fraction. For >80%, this decrease can be well approximated by an empirical exponential decay, providing a simple practical rule for operation. The collection speed is, as expected, also influenced by the magnetic field. Within the explored domain, the time to reach a given collection fraction increases linearly with the magnet-disc gap. Thus, reducing the gap by a factor 3 from 6 mm to 2 mm similarly shortens the 95% collection time from 59 s to 17 s. Finally, comparing configurations shows that switching from a basic design with 4 positions of a permanent magnet stack (Configuration 1) to an alternating pole design with 10 stacks (Configuration 5) further reduces the time to 95% collection from 17 s to 9 s. Overall, the combination of a validated multiphysics model and systematic parameter studies yields transferable design rules that link magnet configuration, magnet–disc distance, and rotational speed to the characteristic time required to reach a targeted bead collection fraction. Beyond the specific implementation studied here, the framework can be adapted to other disc layouts and bead types, providing a practical tool for designing reliable and fast magnetic bead-collection steps in centrifugal microfluidic assays.

Conflicts of interest

There are no conflicts to declare.

Data availability

Data for this article, including the raw data for all figures and results are available at the TU Graz repository DOI: https://doi.org/10.3217/qmwfn-7rj06.

Supplementary information (SI): (1) a description of the lab-on-a-disc prototype; (2) details on the absorption measurements, comprising the disc design used for the calibration as well as the calibration curve itself; (3) the magnetic properties of the beads, including their magnetization curve; (4) a comparison demonstrating the effects of cooperative bead motion with the relative importance of magnetophoresis-induced convection and bead aggregation into chains; and (5) an investigation of the influence of the magnetic field on the particle slip velocity, together with maps of the magnetic flux density for each magnet configuration and for different distances between the magnet ring and the disc. See DOI: https://doi.org/10.1039/d5ra09842d.

Acknowledgements

Supported by TU Graz Open Access Publishing Fund.

Notes and references

1 B. S. Lee, J.-N. Lee, J.-M. Park, J.-G. Lee, S. Kim, Y.-K. Cho and C. Ko, *Lab Chip*, 2009, **9**, 1548–1555.
2 Y.-K. Cho, J.-G. Lee, J.-M. Park, B.-S. Lee, Y. Lee and C. Ko, *Lab Chip*, 2007, **7**, 565–573.
3 S. Lu, Y. Yang, S. Cui, A. Li, C. Qian and X. Li, *Biosensors*, 2024, **14**, 313.
4 H. Yuan, Z. Miao, C. Wan, J. Wang, J. Liu, Y. Li, Y. Xiao, P. Chen and B.-F. Liu, *Lab Chip*, 2025, **25**, 1015–1046.
5 Y. Ha and I. Kim, *BioChip J.*, 2022, **16**, 351–365.
6 M. Wang, L. Jin, P. Hang-Mei Leung, F. Wang-Ngai Chow, X. Zhao, H. Chen, W. Pan, H. Liu and S. Li, *Front. Bioeng. Biotechnol.*, 2024, **12**, 1393789.
7 M. R. Vutukuru, D. K. Sharma, I. Chakraborty, D. Mukhopadhyay and N. Mitra, *Sci. Rep.*, 2025, **15**, 12479.
8 I. Safarik and M. Safarikova, *BioMagn. Res. Technol.*, 2004, **2**, 7.
9 C. Ruffert, *Micromachines*, 2016, **7**, 21.
10 X. Zhuang, Z. Zhao, X. Feng, G. C. Y. Lui, D. Chan, S. S. Lee and I.-M. Hsing, *Anal. Chem.*, 2023, **95**, 6182–6190.
11 D. E. Williams, W. Li, M. Chandrasekhar, C. M. O. W. Corazza, G. S. Deijs, L. Djoko, B. Govind, E. Jose, Y. J. Kwon, T. Lowe, A. Panchal, G. Reshef, M. J. T. Vargas and M. C. Simpson, *Sci. Rep.*, 2024, **14**, 8637.
12 C. Mikkelsen and H. Bruus, *Lab Chip*, 2005, **5**, 1293–1297.
13 A. Munaz, M. J. Shiddiky and N.-T. Nguyen, *Biomicrofluidics*, 2018, **12**, 031501.
14 S. S. Leong, Z. Ahmad, S. C. Low, J. Camacho, J. Faraudo and J. Lim, *Langmuir*, 2020, **36**, 8033–8055.
15 L. Wittmann, E. Krucker-Velasquez, J. Schaupp, L. Westphal, J. W. Swan, A. Alexander-Katz, M. Z. Bazant, S. P. Schwaminger and S. Berensmeier, *Nanoscale*, 2025, **17**, 1574–1584.
16 D. Kirby, J. Siegrist, G. Kijanka, L. Zavattoni, O. Sheils, J. O'Leary, R. Burger and J. Ducrée, *Microfluid. Nanofluid.*, 2012, **13**, 899–908.
17 O. Strohmeier, A. Emperle, G. Roth, D. Mark, R. Zengerle and F. Von Stetten, *Lab Chip*, 2013, **13**, 146–155.
18 S. S. Leong, Z. Ahmad and J. Lim, *Soft Matter*, 2015, **11**, 6968–6980.
19 M. Fratzl, S. Delshadi, T. Devillers, F. Bruckert, O. Cugat, N. Dempsey and G. Blaire, *Soft Matter*, 2018, **14**, 2671–2681.
20 J. Faraudo and J. Camacho, *Colloid Polym. Sci.*, 2010, **288**, 207–215.
21 J. Soika, T. Wanninger, P. Muschak, A. Schnell, S. P. Schwaminger, S. Berensmeier and M. Zimmermann, *Lab Chip*, 2024, **24**, 5009–5019.
22 Y. Ouyang, J. Li, D. M. Haverstick and J. P. Landers, *Anal. Chem.*, 2016, **88**, 11046–11054.
23 S. Hin, N. Paust, M. Rombach, J. Lüddecke, M. Specht, R. Zengerle and K. Mitsakakis, *Micromachines*, 2022, **13**, 2112.
24 Y.-J. Chang, S.-C. Chen and C.-L. Hsu, *Adv. Mater. Sci. Eng.*, 2013, **2013**, 137347.
25 C. R. Phaneuf, B. Mangadu, H. M. Tran, Y. K. Light, A. Sinha, F. W. Charbonier, T. P. Eckles, A. K. Singh and C.-Y. Koh, *Biosens. Bioelectron.*, 2018, **120**, 93–101.

26 A. K. Jahromi, M. Saadatmand, M. Eghbal and L. P. Yeganeh, *Sci. Rep.*, 2020, **10**, 11039.
27 C. M. Miyazaki, E. Carthy and D. J. Kinahan, *Processes*, 2020, **8**, 1360.
28 Thermo Fisher Scientific, M-270 Streptavidin (Dynabeads) — Product information and protocols, 2007.
29 B. Herzog, A. Schultheiss and J. Giesinger, *Photochem. Photobiol.*, 2018, **94**, 384–389.
30 T. G. Mayerhöfer, S. Pahlow and J. Popp, *Chemphyschem*, 2020, **21**, 2029–2046.
31 J. Gómez-Pastora, X. Xue, I. H. Karampelas, E. Bringas, E. P. Furlani and I. Ortiz, *Sep. Purif. Technol.*, 2017, **172**, 16–31.
32 Q. A. Pankhurst, J. Connolly, S. K. Jones and J. Dobson, *J. Phys. D: Appl. Phys.*, 2003, **36**, R167–R181.
33 A. Sinha, Y. Zhang, R. Lednicky, A. Ghaffari and S. Moulton, *Phys. Fluids*, 2007, **19**, 102001.
34 M. Sueptitz, M. Haupt and T. Müller, *Mater. Corros.*, 2013, **64**, 22–31.
35 J. Gómez-Pastora, S. Sanz, M. Barahona and M. Ramos, *J. Phys. Chem. C*, 2017, **121**, 21174–21183.
36 O. Baun and P. Blümler, *J. Magn. Magn. Mater.*, 2017, **439**, 294–304.
37 P. Cregg, K. Murphy and A. Mardinoglu, *Appl. Math. Model.*, 2012, **36**, 1–34.
38 D. T. Grob, N. Wise, O. Oduwole and S. Sheard, *J. Magn. Magn. Mater.*, 2018, **452**, 134–140.
39 J. Andreu Segura, in:*Statistical Mechanics of Superparamagnetic Colloidal Dispersions under Magnetic Fields*, Universitat Autònoma de Barcelona, 2013.
40 M. Grumann, A. Geipel, L. Riegger, R. Zengerle and J. Ducrée, *Lab Chip*, 2005, **5**, 560–565.
41 M. Fermigier and A. P. Gast, *J. Colloid Interface Sci.*, 1992, **154**, 522–539.
42 E. Loth, *Powder Technol.*, 2008, **182**, 342–353.
43 A. D. Grief and G. Richardson, *J. Magn. Magn. Mater.*, 2005, **293**, 455–463.